RSC Advances

PAPER

View Article Online
View Journal | View Issue

Cite this: *RSC Adv.*, 2025, **15**, 17746

Hierarchical porous biomass-derived electrodes with high areal loading for lithium–sulfur batteries†

Qian Wu, Xiaoxin Dou, Fumiao Liu, Jinsheng He, Tinglan Zeng, Tianyu Zeng and Yuanzheng Luo *

Received 6th April 2025
Accepted 14th May 2025

DOI: 10.1039/d5ra02380g

rsc.li/rsc-advances

The natural abundance and environmental benignity of sulfur further endow Li–S batteries with low-cost and green features. The porous structure materials derived from biomass used as sulfur carriers also possess these advantages, making them highly appealing for future high-energy applications. Herein, we utilized chestnut shell carbon (CSC), an inexpensive and readily available agricultural waste, to create a honeycomb-like hierarchical porous carbon for hosting sulfur and a polyacrylonitrile-based graphite fiber (PAN-GF) current collector (CC) to produce an electrode with high areal sulfur loading (10.1 mg cm^{-2}). The CSC@S with aluminum foil CC also exhibited an initial discharge capacity of 1537.7 mAh g^{-1}, with a capacity retention of 70.0% after 100 cycles. The PAN-GF based cathode also could achieve a capacity of over 8.22 mAh cm^{-2} and a volumetric energy density of 366.8 Wh L^{-1}. Beyond conventional aluminum foil coating strategies, this hierarchical porous carbon-embedded fiber structure offers a feasible and cost-effective approach for advancing the development of high-areal sulfur loading electrodes in lithium–sulfur batteries.

1 Introduction

In line with the swift pace of consumer electronics development, lithium-ion batteries (LIBs) have become the most common rechargeable energy storage solution and are extensively used in Electric Vehicles (EVs).[1,2] The rise in popularity of these systems can be attributed to their impressive volumetric energy density, which has led to a significant increase in demand for high-performance energy storage solutions.[3] Currently, the theoretical capacity and energy density of LIBs have reached their limits; the anticipated growth of LIB usage is restrained due to the current limitations in driving range and battery pack size.[4–6] Both issues can be addressed by enhancing energy density at the cell level. Consequently, there is a growing global demand for high-performance batteries. The lithium–sulfur (Li–S) battery is gaining attention as a promising alternative for next-generation energy storage systems. The sulfur cathode is highly favored in electrochemical energy storage for its high theoretical specific capacity (1675 mAh g^{-1}) and high theoretical energy density (2600 Wh kg^{-1}),[7,8] and Li–S batteries have achieved excellent performance using various carbon materials as hosts. Nevertheless, several obstacles must be overcome for further commercial implementations, such as the intrinsic insulating properties of elemental sulfur, along with the "shuttle effect" of the discharge products Li_2S_2 and Li_2S, *etc.* Among these challenges, the cathode porosity (generally > 70%) with nanosized S/C particles also leads to a poor volumetric energy density, and the high content of porous carbon or carbon nanotubes hinders their practical application.[9]

In traditional porous electrode materials, carbon and sulfur particles are nanosized and processed with a solid-slurry technique, resulting in a thickness of 20–50 μm cathode, which is typically coated onto a metal current collector to form a complete cathode structure.[10] Traditional current collectors offer excellent cycling stability and high specific capacity; however, their thickness limitations result in low area density of active material, which constraint limits their capacity and makes it challenging to meet the increasing demand for high-energy density storage solutions.[11,12] To address this issue, researchers have designed freestanding high-areal sulfur loading electrode without metal collectors to achieve higher energy density by increasing the active material loading per unit area.[13] Some researchers have proposed converting planar current collectors into 3D current collectors with interconnected macropores and thick structures, such as copper foam,[14] alloy foam,[15,16] and polymer-derived carbon frameworks.[17] Compared to traditional electrodes, high-areal sulfur loading not only enables Li–S batteries to achieve higher volumetric energy density but also improve battery performance and increase specific capacity. Liu *et al.*[18] has prepared high-areal sulfur loading electrodes by attaching sulfur particles to macroscopic fibres using heavy and dense sulfur-host materials, successfully fabricating dense sulfur cathodes. High-areal

Guangdong Ocean University, Zhanjiang, 524088, Guangdong Province, China. E-mail: luoyz@gdou.edu.cn

† Electronic supplementary information (ESI) available. See DOI: https://doi.org/10.1039/d5ra02380g

sulfur loading electrodes are known to have high sulfur loading capacity. Hierarchical porous carbon can significantly enhance volume energy density when paired with macroporous fibre materials.

Among various sulfur-carrying fibre materials, polyacrylonitrile-based graphite fiber (PAN-GF) stands out due to its excellent conductivity and flexible mechanical strength. This material effectively mitigates the volume expansion issue associated with sulfur, making it a promising choice for macro fibre sulfur host materials in recent developments.[19,20] Wang *et al.*[21] prepared conductive polymer/sulfur composites by heating a mixture of polyacrylonitrile (PAN) and sublimed sulfur. The specific capacity achieved 850 mAh g^{-1} in the first cycle and remained above 600 mAh g^{-1} after 50 cycles, with a sulfur utilization rate of approximately 90%. Liu *et al.*[19] made exciting strides in lithium–sulfur batteries by developing GF/SPAN collector fluids, demonstrating that GF/SPAN electrodes can effectively support higher sulfur loads with improved energy density and cycle stability. Lu *et al.*[20] developed a free-standing 3D-MPGF that exhibits excellent electrochemical properties under various sulfur loads, including low density, high specific capacity, and good cycle stability. These prepared GF/S composites are suitable for use as the cathode in high-performance lithium–sulfur batteries, featuring high sulfur loading capacity, excellent surface loading capability, and good flexibility.

On the other hand, natural biomass materials are eco-friendly and plentiful but affordable and accessible! They feature a versatile porous structure, intricate composition, and diverse functional groups.[22,23] Recently, biomass materials from plants, animals, and microorganisms have been used to create inorganic compounds for lithium–sulfur (Li–S) batteries.[24] Sustainable carbon from agricultural waste (AW) can reduce the "shuttle effect" and enhance the electrochemical activity of the positive electrode. Examples include corncobs, grapefruit peels, coconut shells, shrimp shells, and soybean shells.[25] Elizabeth *et al.*[26] introduced nitrogen-doped porous carbon (PSC) from shrimp shells, which are high in chitin. However, processing shrimp shells is time-consuming and costly. Using agricultural plant waste for biomass-derived carbon is a more eco-friendly and convenient alternative. Yangdan *et al.*[27] used corn cob, an inexpensive waste material, as a carbon source to create a high-performance, spongy, and porous cathode. Although the AW-derived porous carbon (AWPC) can enhance the capacity of lithium–sulfur batteries while maintaining a relatively stable (up to 1073.2 mAh g^{-1} at 0.1C, with efficiency of 99%), a drawback is that these AW-derived porous carbons cannot be utilized to create high-areal sulfur loading electrode materials.

Herein, we presents an innovative approach to attaching hierarchical porous AWPC derived from chestnut shells to macroscopic PAN-GF to fabricate flexible and freestanding cathodes for Li–S batteries. The CSC@S/PAN-GF cathode acts as a collector sulfur-carrying "skeleton" that can series dispersed and disordered dense AWPC carbon, making the ion transport path more coherent. The resulting freestanding flexible battery achieves a capacity of over 8.22 mAh cm^{-2} and a volumetric energy density of 366.8 Wh L^{-1}. Initial discharge capacity at 0.1C reached 950.8 mAh g^{-1}, and stabilized at 98%. At the same time, sulfur loading up to 10.1 mg cm^{-2}. This environmentally friendly cathode preparation process and design strategy demonstrates the potential to enhance lithium–sulfur batteries' volumetric energy density with hierarchical porous AWPC.

2 Experimental section

2.1 Materials and chemicals

The polyacrylonitrile-based graphite fiber (PAN-GF) was purchased from Qingdao Beihai Carbon Co. The composition of PAN-GF consists of 99.99% carbon and has a density of 0.1 mg cm^{-3}. Sulfur powder 99.99% and KOH were purchased from Aladdin Biochemical Technology Co. HCl was purchased from Shenzhen Bolinda Technology Co. Polyethylenimine was purchased from Shanghai McLean Biochemical Technology Co. Chestnut shells were purchased from a local farm.

2.2 Preparation of CSC@S composites

First, waste chestnut shells (CS) were broken into small pieces, each cut into two halves. These pieces were then subjected to alternating ultrasonic washing with pure water and anhydrous ethanol multiple times to remove surface residues of grease and water-soluble impurities. After washing, the shells were immersed in a 20% wt KOH solution for 12 hours and subsequently dried. Song *et al.*[24] conducted an analysis of the supernatant using UV-visible spectroscopy, which revealed that the absorbance reached its lowest point at 600 °C. This finding indicates that the CSC prepared at this temperature exhibits the most effective adsorption properties for Li_2S_2 and Li_2S, as well as an optimal ratio of oxygen and nitrogen doping. As a result, the CSC prepared at 600 °C was selected for subsequent experiments.

Therefore, the pretreated CS were heated for activation and carbonization at 600 °C for 3 h in an Ar atmosphere, with a heating rate of 5 °C min^{-1}. After naturally cooling to room temperature, the material was treated with HCl (1 mol L^{-1}) and washed with deionized water until a neutral pH (pH = 7) was achieved. The material was then filtered and dried to obtain CSC powder.

Afterward, the prepared CSC powder and sulfur were mixed in a weight ratio of 1 : 3 and thoroughly blended by ball milling. The mixture was then heated in a tubular furnace at 155 °C under an Ar gas flow for 12 h, followed by further heating to 240 °C for 30 minutes to remove any excess sulfur. The final sample was cooled in the furnace to room temperature and ground to obtain the CSC@S powder. Fig. 1(a) illustrates the detailed procedure for synthesizing CSC and CSC@S.

2.3 Preparation of the electrodes

The prepared CSC@S material, polyvinylidene difluoride or carboxymethyl cellulose (PVDF/CMC), and Super-P were weighed at 20 mg in a mass ratio of 8 : 1 : 1, then mixed and ground with the dropwise addition of *N*-methyl-2-pyrrolidone (NMP). The resulting mixture was stirred using a vacuum stirrer until a uniform, dense slurry was achieved.

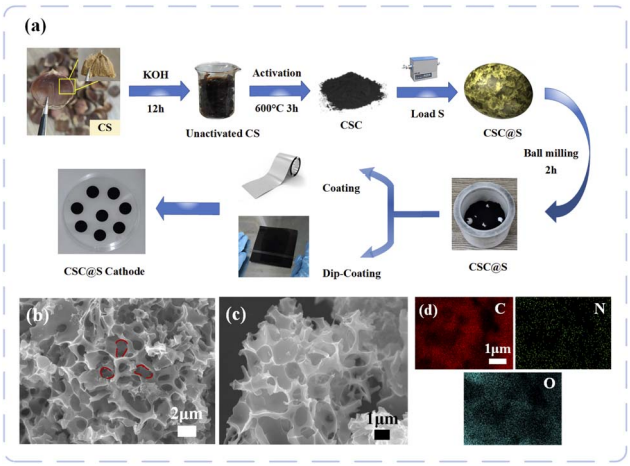

Fig. 1 (a) The schematic illustration showing the preparation of agricultural waste (AW) CSC@S cathode. SEM image of (b) CS. (c) CSC. (d) Elemental mapping of CSC.

In order to prepare the electrode with PAN current collector, the prepared slurry was evenly applied to the PAN-GF substrate through dip-coating. The sample was subjected to a negative pressure environment and vacuum-stationed for 2 h to enhance the capillary action within the PAN-GF, enabling better penetration of the slurry into the fiber structure. Then the whole substrate filled with slurry was dried in a vacuum oven at 60 °C for 8 h and cut into discs with a diameter of 12 mm to obtain the CSC@S/PAN-GF cathode.

In order to prepare the traditional electrode with Al current collector, the prepared slurry was evenly coated onto the Al foil using coaters with sizes of 50 μm, 75 μm, and 250 μm, respectively. The coating foil was then dried in a vacuum oven at 60 °C for 12 h. After the electrodes were thoroughly cooling to room temperature, they were cut into discs with a diameter of 12 mm, resulting in CSC@S/Al-50, CSC@S/Al-75, and CSC@S/Al-250 positive electrodes.

All of the above experiments included electrochemical performance tests, three repeats were performed.

2.4 Material characterization

The microstructure and morphology of the prepared CSC@S composite material were characterized using scanning electron microscope (SEM, JEOL JSM-6510) and transmission electron microscope (TEM, FEI Tecnai G2 F20). The microstructure of the PAN-GF surface was characterized using scanning electron microscopy (SEM, JEOL JSM-6510). The sulfur and carbon content of the samples was analyzed through Thermogravimetric analysis (TGA, METTLER). The composition of the materials was analyzed through energy-dispersive spectroscopy (EDS). X-ray diffraction (XRD, Rigaku SmartLab SE) was employed to analyze the crystal structure and phase composition of materials. The specific surface area and pore size distribution of the products were tested by recording N2 adsorptiondesorption isotherms at 77.3 K using a Brunauer–Emmet–Teller (BET, 3H-2000PS2) instrument. An ultravioletvisible (UV-vis) spectrometer (Lambda 750) was used to verify the adsorption performance of the sulfur host for polysulfides.

2.5 Electrochemical characterization

The CR2032 type button cell was assembled in a glovebox (Vigor SciLab) under an atmosphere filled with Ar and used for electrochemical characterization, as indicated in Fig. S1.† The above-prepared CSC@S anode wafers were used as the cathode and lithium wafers as the anode, which were separated using a Celgard 2400 separator. The electrolyte consisted of 1 M lithium bis (trifluoromethane sulfonyl) imide (LiTFSI) dissolved in a binary solvent mixture of 1,3-dioxolane (DOL) and 1,2-dimethoxyethane (1 : 1 by volume), with 1 wt% $LiNO_3$ as an additive. A 20 μL aliquot of the electrolyte was then added to each cell. Constant current charge–discharge tests were performed using a LAND battery tester within a voltage range of 1.65–2.7 V. The electrochemical performance of the battery was assessed using a CHI660E electrochemical workstation. For Cyclic Voltammetry (CV) measurements, the voltage range was set between 1.65 and 2.7 V, with a scan rate of 100 mV s^{-1} and a current range of ±100 mA. Electrochemical Impedance Spectroscopy (EIS) was performed over a frequency range from 10 mHz to 100 kHz.

3 Results and discussion

3.1 Material characterization

The detailed synthesis procedures of the CSC@S cathode, which utilizes agricultural waste chestnut shell (CS), typically consist of four parts, as shown in Fig. 1(a). CS is derived from the nut of the chestnut genus in the Fagaceae family. It primarily comprises cellulose, lignin, and polysaccharides, with cellulose and lignin accounting for approximately 50–60% of its total mass.[28] The unique structure of CS promotes the formation of a stable three-dimensional network. After ultrasonic washing and soaking, the color of CS faded, and the residual oil on its surface was washed away. The pretreated CS was then activated by soaking in KOH and carbonized at 600 °C, resulting in the formation of a large number of hierarchical porous structures, which were uniformly distributed but exhibited varying pore sizes. The CSC derived from chestnut shells provides a structural foundation for sulfur incorporation, and its unique hierarchical porous structure demonstrates the sulfur-carrying capacity of CS-derived hierarchical porous carbon.

SEM observed the morphology of the CSC structure. Following activation with 20 wt% KOH, the CS was etched to form a porous structure, as shown in Fig. 1(b). As a result of the relatively mild activation process with a low KOH concentration, the macroporous surface structure of CS that resembled a lotus root, with mesopores nested within the macropores. The carbon structure remained continuous and intact.[29] As shown in Fig. 1(c), the activated CSC exhibits a honeycomb-like morphology with thin and irregular pore walls. This structure results from the reaction between KOH and the carbon material during carbonization at 600 °C, which produces gaseous

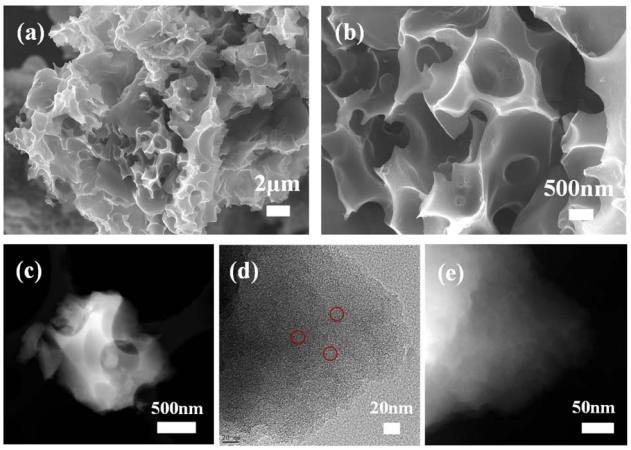

Fig. 2 SEM images of (a and b) CSC@S TEM images of (c–e) CSC@S.

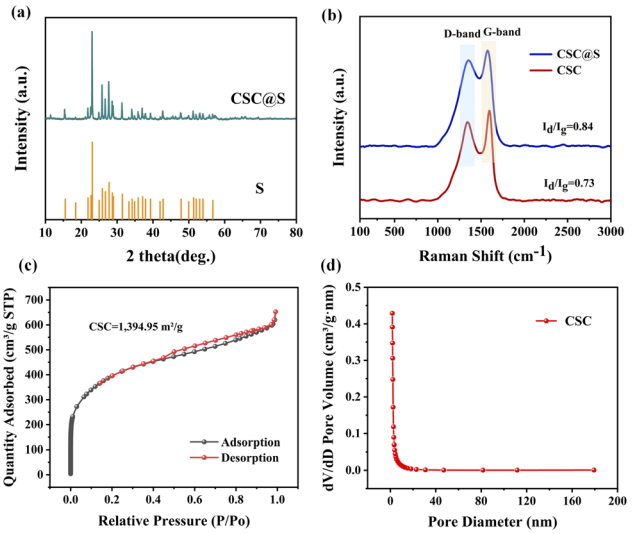

Fig. 3 (a) XRD patterns of CSC@S (b) Raman spectra of CSC and CSC@S (c) nitrogen adsorption/desorption isotherm curves, and (d) pore size distribution curves of CSC.

byproducts that contribute to pore formation.[22,24] The EDS element mapping reveals that the carbonized CSC contains trace elements O and N, indicating that there might be O- and N-related functional groups in the CSC,[24,30,31] as shown in Fig. 1(d). These trace elements are incorporated into the CSC structure during carbonization, not only facilitating the anchoring of S but also enhancing the interaction between S and CSC functional groups.[24] Moreover, the source material CS is naturally abundant, inexpensive, and readily available, which would be favorable for the large-scale and sustainable production of the batteries.

The morphology of the CSC@S structure was observed by SEM, as shown in Fig. 2(a). The surface of CSC@S features numerous interconnected and irregular pore structures of varying sizes, which create potential channels for ion transport. Fig. 2(b) provides a smaller view of the morphological structure. Notably, large pores are uniformly distributed on the CSC surface, which facilitates the accommodation of a significant amount of sulfur, confirming the complex 3D hierarchical porous structure of CSC. This structure is advantageous for integrating flexible collector materials, enabling the fabrication of high-areal sulfur loading electrodes. The TEM micrographs show the presence of many micropores in CSC@S. These micropores help effectively limit polysulfide shuttling and mitigate the aggregation of sulfur particles,[24] as illustrated in Fig. 2(c) and (d). Additionally, the relatively thin pore walls of the CSC material are in the same line with the results of SEM, as shown in Fig. 2(e).

The XRD pattern of CSC@S is shown in Fig. 3(a). CSC@S exhibits a series of characteristic peaks corresponding to sublimed S (JCPDS No. 78-1889) that appear near 23°. After high-temperature carbonization activation, most of the sulfur is attached to the surface of the CSC@S macropores, which is further supports the hierarchical porous carbon nature of the CSC. The degree of graphitization in both the CSC and CSC@S materials was investigated by Raman spectrophotometer, as shown in Fig. 3(b). The D band originated due to structural defects and out-of-plane hybridized carbon atoms, while the G band is a result of in-plane vibrations of sp_2 hybridized carbon atoms.[32,33] For the CSC@S sample, the D and G bands appear at 1374 cm^{-1} and 1582 cm^{-1}. An increase in the I_d/I_g ratio implies the defects and deformation of sp_2 hybridized carbon atoms.[34,35] The I_d/I_g ratios for CSC and CSC@S are 0.73 and 0.84, respectively. The higher value of I_d/I_g for CSC@S indicates that its carbon structure is more disordered.

To investigate the specific surface area and pore size distribution of CSC materials, Brunauer–Emmett–Teller (BET) analysis was performed. The porous characters of the CSC materials were examined by N_2 adsorption/desorption, as illustrated in Fig. 3(c). The CSC isotherm displays a hysteresis loop at a relative pressure (P/P_0) of approximately 0.45. According to IUPAC classification, CSC showed a clear combination of type-I and type-IV adsorption/desorption isotherms, indicating the coexistence of microporous and mesoporous structures in CSC.[27] Fig. 3(d) illustrates the bimodal pore size distribution curve of CSC, which reveals a significant number of micropores (<2 nm) and some mesopores (2–50 nm). This indicates that the CSC material has a hierarchical porous structure. The specific surface area of the CSC was calculated using the BET method to be 1394.95 $m^2\ g^{-1}$, with a pore volume of 1.01 $cm^3\ g^{-1}$. The results showed that KOH successfully activated the formation of the porous structure in CSC, effectively increasing the specific surface area of the material and providing more active sites for reactions.[24]

The fiber structure of PAN-GF effectively encases the CSC hierarchical porous carbon, as depicted in Fig. 4(a). PAN-GF is primarily composed of carbon, which forms a dense and conductive carbon framework for CSC@S. Fig. 4(b) illustrates the surface of the PAN-GF structure, significantly increasing the contact area between the active material and the PAN-GF collector. Based on the CSC@S composite, The PAN-GF material was introduced as the coating collector, which exhibits both flexibility and adsorption properties. Meanwhile, PAN-GF

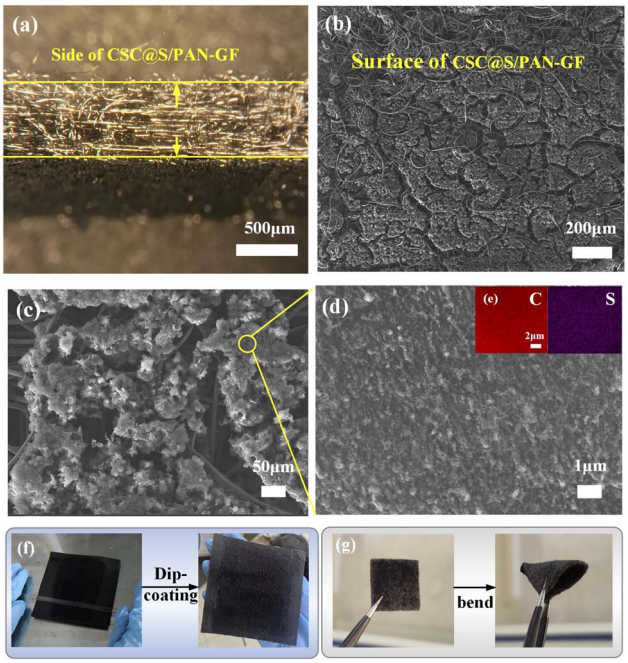

Fig. 4 (a) Cross-sectional image of PAN-GF SEM images of (b–d) PAN-GF (e) elemental mapping of PAN-GF (f) coating process of PAN-GF (g) flexibility test of PAN-GF.

exhibits better tensile properties, as shown in Fig. S2.† Fig. 4(c) shows the SEM micrograph of PAN-GF, revealing a loose and foamy 3D network structure on the surface, interwoven with fine fibers. This structure provides numerous attachment sites for the CSC hierarchical porous carbon, potentially enhancing the electrochemical reaction rate.[19,36] In contrast to the smooth, two-dimensional surface of traditional aluminum foil, the complex three-dimensional network of PAN-GF exhibits superior adsorptive qualities. Upon magnification, the surface of the PAN-GF fibers appears rough, as illustrated in Fig. 4(d). This intricate 3D network serves as a sulfur-carrying scaffold, efficiently dispersing and accommodating the densely packed CSC while promoting better adsorption of sulfur-active substances and the electrolyte. Elemental mapping is shown in Fig. 4(e), indicates the presence of trace elements such as S in PAN-GF. This increased contact area enhances the adsorption of the active material, thereby improving the cycling stability of Li–S batteries.[19,36] Unlike traditional aluminum/copper electrode coatings that utilize a scraper or coater, the PAN-GF collector requires a glass rod to press the active material into the fibers, ensuring that the material is well-adsorbed within the PAN-GF structure, as shown in Fig. 4(f). Flexibility tests on the PAN-GF material showed that the PAN-GF coated with the CSC@S active substance demonstrated high flexibility, exhibiting no visible fractures or breakage on the surface of the collector, as shown in Fig. 4(g).

3.2 Electrochemical analysis

CSC@S samples were used to coat aluminum foil collectors with thicknesses of 50 μm, 75 μm, and 250 μm, respectively.

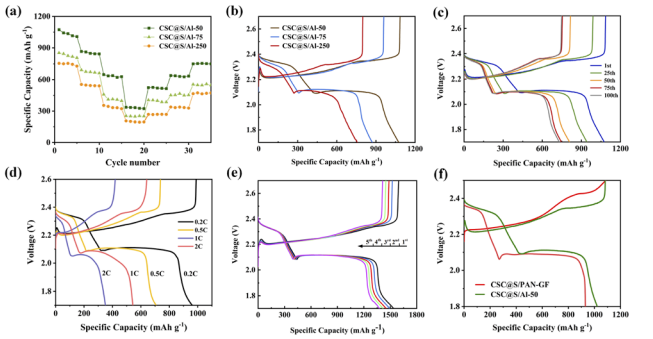

Fig. 5 (a) Rate capability of CSC@S/Al cathode with 50 μm, 75 μm and 250 μm thicknesses charge–discharge cycles of (b) CSC@S/Al cathode with 50 μm, 75 μm and 250 μm thicknesses. (c) CSC@S/Al-50 cathode for 100 cycle (d) CSC@S/Al-50 cathode at 0.2C, 0.5C, 1C and 2C, respectively (e) the first five charge/discharge cycles of CSC@S/Al-50 cathode at 0.1C (f) CSC@S/PAN-GF with CSC@S/Al-50 cathode at 0.1C.

Additionally, CSC@S samples were applied to coat PAN-GF collectors in order to prepare thicker electrodes. Both types of collector electrodes underwent electrochemical testing and performance comparisons. In all electrochemical analyzes, three repetitions were performed.

To evaluate the rate performance, the CSC@S coated with aluminum foil of varying thicknesses cathode is tested at different current density, as shown in Fig. 5(a). The cycle rate performance of the cells decreases as the coating thickness increases, particularly with higher discharge capacity. The CSC@S/Al-50 cathode demonstrates superior performance across all cycle rate performance. The corresponding initial capacities were 993.2 mAh g^{-1}, 865.7 mAh g^{-1}, 648.2 mAh g^{-1}, and 336.1 mAh g^{-1}, respectively, at 0.2C, 0.5C, 1C, and 2C. When cycled back to 0.2C, the discharge capacity recovered to 755 mAh g^{-1}, resulting in a capacity retention of 76%. In contrast, the CSC@S/Al-75 and CSC@S/Al-250 cathodes retained only 65% and 61.6% of their initial capacities, respectively, at the same discharge capacity. The initial discharge capacities of the CSC@S/Al cells at different thicknesses were 1073.2 mAh g^{-1}, 830.2 mAh g^{-1}, and 511.5 mAh g^{-1} at 0.1C. As illustrated in Fig. 5(b), the CSC@S/Al-50 cells outperformed the CSC@S/Al-75 and CSC@S/Al-250 cells. This indicates that thicker aluminum foil negatively impacts the interaction between the electrode material and the electrolyte, leading to a degradation in performance. Therefore, electrodes with aluminum as the current collector should be coated with thin layers to ensure optimal cell performance. Additionally, these results demonstrate the feasibility of utilizing sulfur extracted from CS hierarchical porous carbon in cells with collectors of varying thickness.

After 100 cycles, the CSC@S/Al-50 cell retained a capacity of 752.1 mAh g^{-1}, as shown in Fig. 5(c). The charge/discharge curves for the CSC@S/Al-50 at 0.2C, 0.5C, 1C, and 2C are displayed in Fig. 5(d). At a 0.2C rate, the initial discharge capacity reached 993.2 mAh g^{-1}. As the discharge rate increased, both the specific discharge capacity and the discharge plateau of the

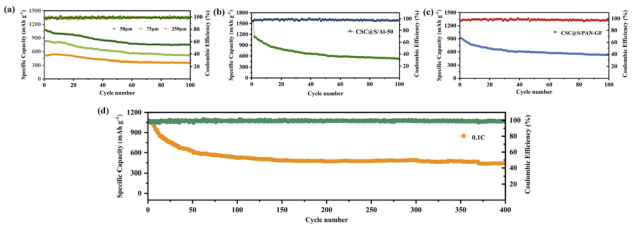

Fig. 6 (a) Cycling performance of CSC@S/Al cathode with 50, 75 and 250 μm thicknesses at 0.1C (b) cycling performance of CSC@S/Al-50 cathode for 100 cycle (c) cycling performance of CSC@S/PAN-GF cathode at 0.1C (d) cycling performance of CSC@S/Al-50 cathode for 400 cycle at 0.1C.

cell gradually decreased, with the discharge plateau curve becoming more curved. This trend indicates a deterioration in discharge stability, which is consistent with the results from the cycle rate performance. The first five charge/discharge cycles of the CSC@S/Al-50 cell at 0.1C are shown in Fig. 5(e). Its initial discharge capacity was 1537.7 mAh g^{-1}, representing 93.1% of the theoretical capacity of the Li–S battery (1650 mAh g^{-1}). After five cycles, the capacity retention of the CSC@S/Al-50 was 88.8%. The discharge plateau remained broadly consistent, indicating strong discharge stability, sustained capacity, and excellent electrochemical performance. This observation aligns with the data on cycling performance and coulombic efficiency (CE). Fig. 5(f) presents the charge/discharge curves for the CSC@S/PAN-GF and CSC@S/Al-50 cells at 0.1C. The initial discharge capacity of the PAN-GF collector cell was 912.5 mAh g^{-1}, which is higher than CSC@S/Al-50 cell. The discharge plateau for the CSC@S/PAN-GF cell remained stable, exhibiting two distinct potential platforms that correspond with the CV results, reflecting the terrific electrochemical stability of the CSC@S/PAN-GF cell.

Fig. 6(a) presents the discharge curves of CSC@S with coating thicknesses of 50 μm, 75 μm, and 250 μm after 100 cycles at 0.1C. The CSC@S/Al-50 cell exhibited an initial discharge capacity of 1073.2 mAh g^{-1}, which corresponds to 64% of the theoretical capacity of Li–S batteries. The CSC@S cells with varying thicknesses demonstrated stable performance for 100 cycles, highlighting the potential of CSC hierarchical porous carbon as an effective sulfur carrier in Li–S batteries. Fig. 6(b) displays the discharge curves of CSC@S/Al-50 for 100 cycles at 0.1C. The initial capacity reached 1563.7 mAh g^{-1}, with the CE stabilizing at 96%. After 100 cycles, the capacity declined to 526.7 mAh g^{-1}. This performance can be attributed to the diverse functional groups in the CSC material that form hydrogen bonds with water molecules, promoting smooth progression of the electrochemical reactions. Fig. 6(c) presents the discharge curve for CSC@S/PAN-GF for 100 cycles at 0.1C. The initial cyclic discharge capacity of CSC@S/PAN-GF reached 950.8 mAh g^{-1}, with CE stabilizing at approximately 98%. Moreover, the strong adsorption capability of the PAN-GF electrode enhances the retention of the CS carbon. The combination of CSC and PAN-GF structures provides a continuous electron transport pathway, effectively reducing interfacial resistance.[37] Additionally, PAN-GF adsorption property improves slurry retention, significantly decreasing interfacial resistance and enhancing the volumetric energy density of CSC@S/PAN-GF cells to as high as 90 mg cm^{-3}. The strong adsorption and three-dimensional structure of PAN-GF, coupled with the graded porous structure of CSC sulfur carriers, contribute to stable performance under high sulfur loading.[37,38] Fig. 6(d) presents the discharge curve for CSC@S/Al-50 for 400 cycles at 0.1C. After 400 cycles, the cell retains a discharge capacity of 442.2 mAh g^{-1}, demonstrating strong cycling stability. This further proves the feasibility of the CS-derived AWPC cell.

The results indicate that with the increase in current collector thickness, the sulfur loading capacity gradually improves, leading to enhanced energy density and cycle stability of the battery. This may be attributed to the fact that thicker current collectors can mitigate the volumetric expansion of sulfur during charge–discharge cycles.[39] However, the increase in thickness also introduces drawbacks. For instance, in Al cathode, as the thickness increases, the battery's capacity and discharge rate gradually decrease, which may be due to the increased internal resistance of the thicker current collector, hindering the transport of lithium ions. Therefore, selecting an appropriate current collector and designing an optimal thickness is crucial for enhancing the electrochemical performance of lithium–sulfur batteries. In conclusion, the aluminum foil and PAN-GF collectors exhibit superior electrochemical performance.

Fig. 7(a) illustrates the areal capacity of the CSC@S material based on PAN-GF and Al (50 nm) at a current density of 3 mA cm^{-2}. The sulfur surface loading of the CSC@S/PAN-GF electrode reaches 10.1 mg cm^{-2} at 0.1C. It demonstrates the high sulfur loading capacity of PAN-GF. Meanwhile, the high surface loading of sulfur lays the foundation for the relatively high volumetric energy density of the CSC@S/PAN-GF battery. In contrast, the sulfur surface loadings for the CSC@S/Al-50, CSC@S/Al-75, and CSC@S/Al-250 electrodes are 1.7, 1.7, and 1.9 mg cm^{-2}, respectively, at 0.1C, as shown in Fig. 7(b). This means that the sulfur surface loading of the PAN-GF electrode is approximately 5 to 6 times higher than that of the conventional CSC@S/Al electrode. A comparison of the electrochemical

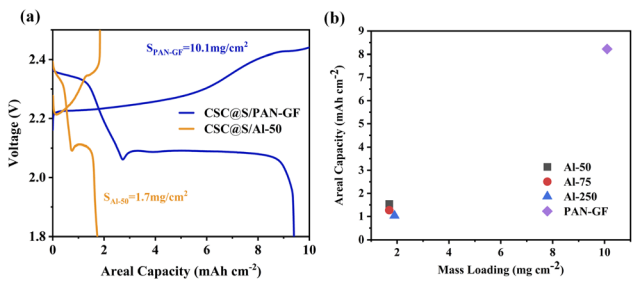

Fig. 7 (a) Charge/discharge profiles for CSC@S/PAN-GF and CSC@S/Al-50 cathodes at an areal current density of 3 mA cm^{-2}. (b) Comparison of areal capacity between CSC@S/Al cathodes with thicknesses of 50 μm, 75 μm and 250 μm, and CSC@S/PAN-GF cathodes.

Table 1 Comparison of the capabilities of PAN-GF and Al collector for 100 cycles at 0.1C

	Specific capacity (mAh g^{-1})		Efficiency (%)			
Sample (0.1C)	1st	100th	1st	100th	Capacity retention rate (%)	Sulfur surface load (mg cm^{-2})
CSC@S/PAN-GF	950.8	530.1	96.5	97.1	55.7	10.1
CSC@S/Al-50	1563.7	526.7	98.1	98.4	33.6	1.7
CSC@S/Al-75	830.2	514.0	96.1	99.4	61.9	1.7
CSC@S/Al-250	511.5	357.7	98.5	98.6	69.9	1.9

capacities of the PAN-GF and Al collector electrodes for 100 cycles at 0.1C is shown in Table 1.

Compared to CSC@S/Al-50, CSC@S/Al-75, and CSC@S/Al-250, the CSC@S/PAN-GF battery exhibits a faster capacity decay. By comparing the Al current collector and the PAN-GF current collector, it was found that the rapid capacity decay is due to the inferior conductivity of the PAN-GF current collector compared to the Al current collector.[40]

The following is the procedure for calculating the volumetric energy density of the CSC@S/PAN-GF cell:

$$Q = \frac{L}{h} \quad (1)$$

where Q is the volumetric capacity (mAh cm^{-3}), L is the capacity loading (mAh cm^{-2}), and h is the thickness of the electrode layer (cm). In the constant current charge–discharge tests, we get $h = 0.224$ mm and $L = 8.22$ mAh cm^{-2}.

In eqn (1), we get $Q \approx 366.8$ Wh L^{-1}.

The CV curves of the CSC@S/Al-50 cell, obtained after 100 charge/discharge cycles at 0.1C, are shown in Fig. 8(a). At a scan rate of 0.1 mV s^{-1}, the CV curve exhibits a prominent reduction peak near 2.0 V, typically attributed to the cleavage of the S_8 ring and the conversion of long-chain lithium polysulfides to short-chain lithium polysulfides.[32] Another reduction peak around 2.3 V corresponds to the conversion of short-chain polysulfides to the final discharge products. During the charging scan, an oxidation peak appears near 2.4 V. After four cycles, the cell shows a trend of decreasing and increasing reduction peaks, indicating a reduction in internal polarization and improved active material utilization.[41] Fig. 8(b) presents the CV curves of the CSC@S/PAN-GF cell after four cycles of 100 charge/discharge tests at 0.1C. The discharge scan of the CSC@S/PAN-GF cell shows distinct reduction peaks at approximately 2.0 V and 2.3 V, while the oxidation peak appears near 2.4 V during the charge scan. After four cycles, the oxidation and reduction peaks' positions remained unchanged, demonstrating the excellent stability of the PAN-GF material.

EIS was performed on different electrodes, and the corresponding Nyquist plots and fitted circuits are presented in Fig. 8(c)–(e). The first semicircle is due to the SEI layer and the second semicircle is due to charge transfer at the electrolyte and electrode interface.[19] As shown in Fig. 8(c), the CSC@S/Al-75 electrode exhibits lower charge transfer impedance (R_{ct}) and solution resistance (R_s) compared to the CSC@S/Al-50 cathode in the high-frequency region. W_1 represents the diffusion resistance in the low-frequency region in the fitted circuit. The W_1 values for both electrodes are similar, likely due to their slight difference in thickness. In Fig. 8(d), CSC@S/Al-250 demonstrates a higher R_s than CSC@S/Al-50 in the high-frequency region, but its R_{ct} is lower. This can be attributed to the thicker coating, accommodating more active materials and providing more electrochemical reaction sites. As shown in

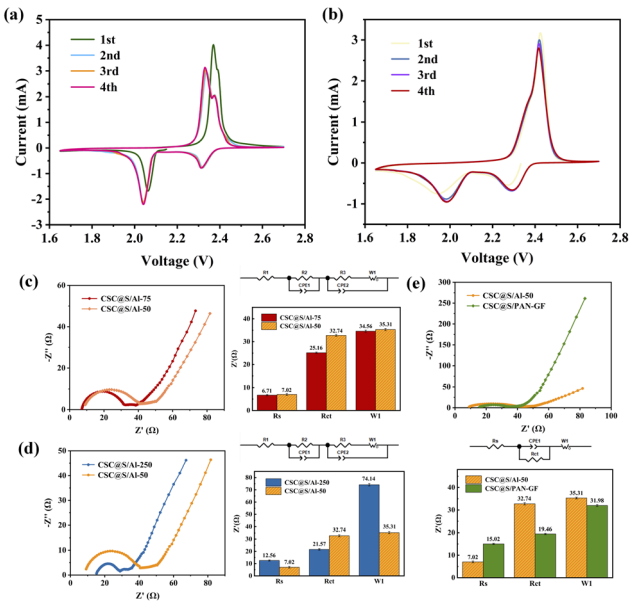

Fig. 8 (a) CV curves of CSC@S/Al cells with 50 μm thickness (b) CV curves of CSC@S/PAN-GF cells different electrodes Nyquist curves and equivalent circuit parameters of electrodes (c) CSC@S/Al-50 and CSC@S/Al-75 (d) CSC@S/Al-50 and CSC@S/Al-250 (e) CSC@S/Al-50 and CSC@S/PAN-GF.

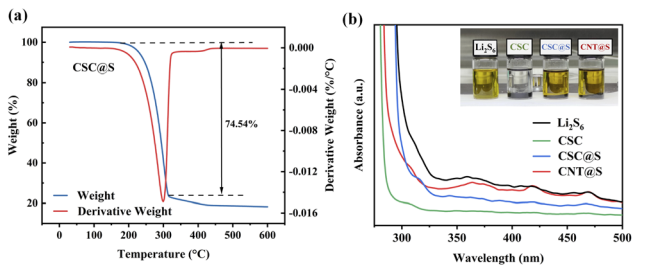

Fig. 9 (a) Thermogravimetric analysis (TGA) of CSC@S. (b) UV-vis spectra of the blank Li_2S_6 solution and Li_2S_6 with CSC, CSC@S and CNT@S samples.

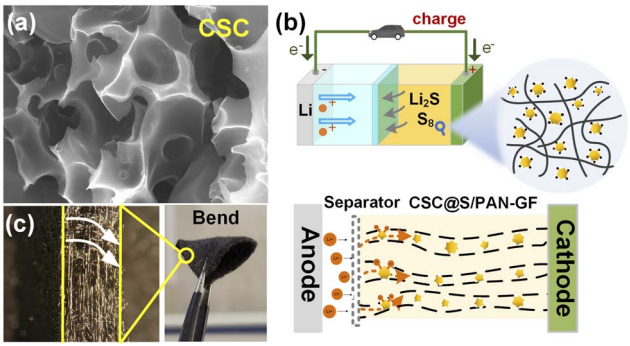

Fig. 10 (a) SEM images of CSC on the PAN-GF surface; (b) mechanism of polysulfide conversion in the CSC@S/PAN-GF electrode; (c) micrographs and photo of the CSC@S/PAN-GF.

Fig. 8(e), the CSC@S/PAN-GF electrode has a lower R_{ct} compared to the CSC@S/Al-50 cathode in the high-frequency region, possibly due to the high tortuosity and fiber structure of the PAN-GF material, which effectively adsorbs more active material slurry. The CSC@S/Al-50 cathode shows lower R_s, likely because the electrode is in close contact with the electrolyte, and the aluminum foil surface has low ohmic resistance when in contact with the electrolyte. Finally, the W_1 value for CSC@S/PAN-GF is higher than that for CSC@S/Al-50, suggesting that the graded porous carbon derived from CS integrates with the three-dimensional fibrous structure of PAN-GF during charge/discharge cycles, forming a continuous ionic diffusion channel that enhances the diffusion process.

Thermogravimetric analysis (TGA) was employed to determine the sulfur content in the CSC@S composite material. The sulfur loading rate of the CSC@S material is 74.54%. Fig. 9(a) shows a characteristic inflection point in the TGA curve of CSC@S around 300 °C, suggesting that, as the temperature rises from room temperature to 300 °C, the unstable sulfur on the surface of CSC evaporates first. After reaching 300 °C, the more stable sulfur within the micropores and mesopores of CSC gradually begins to evaporate. The TGA results confirm the presence of a unique hierarchical porous structure in the CSC material.

The anchoring ability of four materials towards Li_2S_6 was evaluated by adding equal amounts of CSC, CSC@S, and CNT@S to a fixed-volume solution of Li_2S_6, as shown in the Fig. 9(b). After 12 h, CSC completely decolourized the Li_2S_6 solution, while the colour change of CSC@S and CNT@S was less pronounced than that of CSC. Ultravioletvisible spectroscopy (UV-vis) further confirmed that CSC exhibited a strong adsorption capability. Based on the intensity of the spectral signals, the adsorption abilities were ranked from strongest to weakest as CSC > CSC@S > CNT@S.

SEM images (Fig. 10(a)) further verified the above-mentioned results. Fig. 10(b) illustrates the interaction between the nanofiber in CSC@S/PAN-GF and lithium polysulfides to explore the electrochemical mechanism. The shuttling of lithium polysulfides through the pores of CSC@S is restrained due to the physical barrier of the hierarchical porous and fiber structure. More importantly, this unique structure, with high tortuosity, enhances the utilization of sulfur and the cycling stability of the high-areal sulfur loading electrode (Fig. 10(c)). The desirable performance of our nanofiber-enhanced high-areal sulfur loading electrodes illustrates the feasibility of the thick cathode system for practical applications.

4 Conclusions

In summary, the KOH activation method successfully synthesized hierarchical porous chestnut shell carbon materials (CSC). As a bio-derived sulfur host material, when used on aluminum foil, it exhibits an excellent specific capacity of up to 1537.7 mAh g^{-1}, close to its theoretical maximum value; when dip-coated on flexible PAN-GF, it exhibits excellent surface current density and high sulfur loading. By combining hierarchical porous carbon and PAN-GF, the kinetic properties of biomass carbon high-areal sulfur loading electrode are improved. After 100 cycles, it retains a 743.6 mAh g^{-1} capacity, exhibiting nearing 100% and a low decay rate of only 0.74%. Not limited to conventional aluminum foil coating strategies, this novel electrode with hierarchical porous carbon embedded in carbonfiber providing a reference for promoting the practical application of high-areal sulfur loading electrodes. Despite the relatively low polarity of CSC@S/PAN-GF, the host materials play a crucial role in LSBs. Our porous carbon/PAN-GF framework offers excellent electrical conductivity, a high specific surface area, and a significant sulfur loading capacity. Additionally, its unique structure allows for the incorporation of embedded high polarity catalysts or other catalytic materials on the surface of these porous carbon/fiber hybrid host materials, enabling potential applications in the future.

Data availability

Data is provided within the manuscript or ESI files.†

Conflicts of interest

There are no conflicts to declare.

Acknowledgements

The authors acknowledge the support from the "Guangdong Basic and Applied Basic Research Foundation" (Grant No. 2023A1515010590), and Guangdong Provincial Key Laboratory of Intelligent Equipment for South China Sea Marine Ranching, Guangdong Ocean University, Zhanjiang 524088, China, and the authors acknowledge the support from the Undergraduate Innovation Team Project of Guangdong Ocean University (CXTD2024014).

Notes and references

1 Y. Huang, R. Field, Q. Chen, Y. Peng, M. S. Walczak, H. Zhao, G. Zhu, Z. Liu and L. Li, *Commun. Chem.*, 2019, **2**, 138.

2 N. Nakamura, S. Ahn, T. Momma and T. Osaka, *J. Power Sources*, 2023, **558**, 232566.
3 Q. Zhang, Q. Huang, S.-M. Hao, S. Deng, Q. He, Z. Lin and Y. Yang, *Adv. Sci.*, 2022, **9**, 2103798.
4 Z. Zhou, P. Lin, S. Zhao, H. Jin, Y. Qian, X. Chen, X. Tang, Q. Zhang, D. Guo and S. Wang, *Small*, 2022, **18**, 2205887.
5 W. Wang, W. Dong, X. Hong, Y. Liu and S. Yang, *Mater. Chem. Phys.*, 2022, **283**, 126014.
6 Y. Lin, L. Li, L. Tan, Y. Li, X. Ren, P. Zhang, C. He and L. Sun, *J. Energy Chem.*, 2024, **95**, 540–553.
7 M. Wang, Z. Bai, T. Yang, C. Nie, X. Xu, Y. Wang, J. Yang, S. Dou and N. Wang, *Adv. Energy Mater.*, 2022, **12**, 2201585.
8 X. Xu, H. Chen, H. Duan, W. Yang, X. Xu, Y. Zou, Z. Ma and W. Lei, *Acta Mater.*, 2023, **260**, 119309.
9 D. S. Baji, S. Kannan, P. B. Madambikattil, A. Thirumurugan, M. K. Sharma, R. K. Pai, A. Ramadoss, S. Nair and D. Santhanagopalan, *J. Energy Storage*, 2024, **100**, 113412.
10 S. Jin, Y. Jiang, H. Ji and Y. Yu, *Adv. Mater.*, 2018, **30**, 1802014.
11 J. Shao, J. Zheng, G. Xing, Y. Lu, X. Lv and C. Zhang, *J. Energy Storage*, 2024, **103**, 114357.
12 T. Wang, Q. Zhang, J. Zhong, M. Chen, H. Deng, J. Cao, L. Wang, L. Peng, J. Zhu and B. Lu, *Adv. Energy Mater.*, 2021, **11**, 2100448.
13 Y. Kuang, C. Chen, D. Kirsch and L. Hu, *Adv. Energy Mater.*, 2019, **9**, 1901457.
14 Z. Lu, Z. Tai, Z. Yu, A. P. LaGrow, O. Bondarchuk, J. P. Sousa, L. Meng, Z. Peng and L. Liu, *Mater. Today Energy*, 2021, **22**, 100871.
15 F. Liu, E. Wang, C. Wu, D. Sun and J. Li, *J. Solid State Electrochem.*, 2021, **25**, 2033–2039.
16 K. Y. Song and S. K. Joo, *Mater. Res. Bull.*, 2017, **94**, 328–334.
17 H. Peng, T. Zhang, W. Shao, S. Liu and F. Hu, *Appl. Surf. Sci.*, 2021, **569**, 150935.
18 Y.-T. Liu, S. Liu, G.-R. Li, T.-Y. Yan and X.-P. Gao, *Adv. Sci.*, 2020, **7**, 1903693.
19 F. Liu, S. Chiluwal, A. S. Childress, C. Etteh, K. Miller, M. Washington, A. M. Rao and R. Podila, *ACS Appl. Nano Mater.*, 2021, **4**, 53–60.
20 L. Lu, J. T. M. De Hosson and Y. Pei, *Carbon*, 2019, **144**, 713–723.
21 J. Wang, J. Yang, C. Wan, K. Du, J. Xie and N. Xu, *Adv. Funct. Mater.*, 2003, **13**, 487–492.
22 J. Liu, H. Yuan, X. Tao, Y. Liang, S. J. Yang, J.-Q. Huang, T.-Q. Yuan, M.-M. Titirici and Q. Zhang, *EcoMat*, 2020, **2**, e12019.
23 A. Feng, X. Zhu, Y. Chen, P. Liu, F. Han, Y. Zu, X. Li and P. Bi, *ChemElectroChem*, 2024, **11**, e202400086.
24 P. Song, L. Han, L. Zhu, R. Zhang, Y. Chai, Z. Lei, L. Wang and S. Shen, *Chem.–Asian J.*, 2023, **18**, e202300604.
25 I. Tunc, B. D. Karahan and O. Keles, *Appl. Phys. A: Mater. Sci. Process.*, 2024, **130**, 677.
26 I. Elizabeth, B. P. Singh, S. Trikha and S. Gopukumar, *J. Power Sources*, 2016, **329**, 412–421.
27 L. Yangdan, G. Yichuan, T. Yang, T. Haichao, Y. Zhizhen and L. Jianguo, *Ionics*, 2022, **28**, 2593–2601.
28 J. M. Yu, M. Nam and M.-S. Kim, *Foods*, 2022, **11**, 1325.
29 H. Liu, W. Liu, F. Meng, L. Jin, S. Li, S. Cheng, S. Jiang, R. Zhou and J. Liu, *Sci. China: Technol. Sci.*, 2022, **65**, 2380–2387.
30 S. Imtiaz, J. Zhang, Z. A. Zafar, S. Ji, T. Huang, J. A. Anderson, Z. Zhang and Y. Huang, *Sci. China Mater.*, 2016, **59**, 389–407.
31 P. K. Nema, K. Mohanty and R. Thangavel, *J. Ind. Eng. Chem.*, 2023, **121**, 235–241.
32 A. Pundir and A. Sil, *Biomass Bioenergy*, 2024, **180**, 106999.
33 M. Zimik, S. Sarmah, B. K. Kakati, D. Deka and R. Thangavel, *Mater. Res. Bull.*, 2024, **180**, 113017.
34 S.-Y. Lee, Y. Choi, J.-K. Kim, S.-J. Lee, J. S. Bae and E. D. Jeong, *J. Ind. Eng. Chem.*, 2021, **94**, 272–281.
35 A. Khan, R. A. Senthil, J. Pan, S. Osman, Y. Sun and X. Shu, *Electrochim. Acta*, 2020, **335**, 135588.
36 G. Hu, C. Xu, Z. Sun, S. Wang, H.-M. Cheng, F. Li and W. Ren, *Adv. Mater.*, 2015, **28**, 1603–1609.
37 K. Wang, S. Ju, Q. Gao, G. Xia, G. Wang, H. Yan, L. Dong, Z. Yang and X. Yu, *J. Alloys Compd.*, 2021, **860**, 158445.
38 J.-W. Park, S.-C. Jo, M.-J. Kim, I.-H. Choi, B. G. Kim, Y.-J. Lee, H.-Y. Choi, S. Kang, T. Kim and K.-J. Baeg, *NPG Asia Mater.*, 2021, **13**, 30.
39 S. Liu, H. Zhang, X. Liu, Y. Yang, C. Chi, S. Wang, J. Xue, T. Hao, J. Zhao and Y. Li, *J. Energy Chem.*, 2021, **58**, 124–132.
40 U. Nisar, N. Muralidharan, R. Essehli, R. Amin and I. Belharouak, *Energy Storage Mater.*, 2021, **38**, 309–328.
41 K. Shwetha, M. S. Kamath, C. K. Rastogi, Y. Athreya, S. Sudhakaran and C. Manjunatha, *J. Energy Storage*, 2024, **97**, 112699.